High performance metal-supported intermediate temperature solid oxide fuel cells fabricated by atmospheric plasma spraying

Chang-sing Hwang [a,∗], Chun-Huang Tsai [a], Jen-Feng Yu [a], Chun-Liang Chang [a], Jun-Meng Lin [a], Yaw-Hwa Shiu [b], Shih-Wei Cheng [b]

[a] *Physics Division, Institute of Nuclear Energy Research, Lungtan, Taoyuan 32546, Taiwan, ROC*
[b] *Nuclear Fuels and Materials Division, Institute of Nuclear Energy Research, Lungtan, Taoyuan 32546, Taiwan, ROC*

ARTICLE INFO

ABSTRACT

The LSGM($La_{0.8}Sr_{0.2}Ga_{0.8}Mg_{0.2}O_3$) electrolyte based intermediate temperature solid oxide fuel cells (ITSOFCs) supported by porous nickel substrates with different permeabilities are prepared by plasma spray technology for performance studies. The cell having a porous nickel substrate with a permeability of 3.4 Darcy, an LSCM($La_{0.75}Sr_{0.25}Cr_{0.5}Mn_{0.5}O_3$) interlayer on the nickel substrate, a nano-structured LDC($Ce_{0.55}La_{0.45}O_2$)/Ni anode functional layer, an LDC interlayer, an LSGM/LSCF($La_{0.58}Sr_{0.4}Co_{0.2}Fe_{0.8}O_3$) cathode interlayer and an LSCF cathode current collector layer shows remarkable electric output power densities such as 1270 mW cm^{-2} (800 °C), 978 mW cm^{-2} (750 °C) and 702 mW cm^{-2} (700 °C) at 0.6 V cell voltage under 335 ml min^{-1} H$_2$ and 670 ml min^{-1} air flow rates. SEM, TEM, EDX, AC impedance, voltage and power data with related analyses are presented here to support this high performance. The durability test of the cell with the best power performance shows a degradation rate of about 3% kh^{-1} at the test conditions of 400 mA cm^{-2} constant current density and 700 °C. Results demonstrate the success of APS technology for fabricating high performance metal-supported and LSGM based ITSOFCs.

© 2010 Elsevier B.V. All rights reserved.

1. Introduction

The solid oxide fuel cell (SOFC) is an electrochemical reactor for generating electricity and has some unique advantages over the traditional power generation technologies, including inherently high efficiency, low gas pollution emissions and fuel flexibility [1–3]. Over the past two decades, technical developments have focused on the development of both advanced SOFC materials and structures so that the reduction of cell operation temperature can be realized [4–8]. SOFCs with reduced operation temperature (600–800 °C) provide numerous advantages such as wider choices of low-cost component materials, improved sealing and interfacial reaction prevention, and increased flexibility in the structure design [9–11].

Toward lowing operation temperatures, there is a tendency to shift ceramic-supported fuel cells to metal-supported fuel cells due to the potential benefits of low cost, high strength, better workability, good thermal conductivity and quicker start-up [12–14]. Quicker start-up and thermal cycling are considered as the main causes of ceramic-supported fuel cell breakage and stack failure [15,16]. Metal-supported fuel cells are desired to be used in the auxiliary power unit of mobile application where the structural robustness and the thermal shock resistance with low internal temperature and stress gradients are required [17,18]. In addition, metallic substrates allow the use of conventional metal welding techniques for stack sealing and could significantly reduce the manufacturing costs of SOFC stacks.

SOFCs are typically manufactured using wet ceramic techniques such as tape casting combined with multi-steps of high temperature (up to 1400 °C) sintering to obtain dense electrolytes. It is difficulty to incorporate metallic substrates into the wet ceramic manufacturing processes without oxidizing the metallic substrates or significantly changing metallic substrate properties. In the case of the metal substrates showing only reduced or no shrinkage during co-firing processes, it is troublesome to obtain dense electrolytes. Plasma spray processes do not need the shrinkage of substrates and are favorable for the coating of substrates with reduced shrinkage as used in the metal-supported fuel cells. Plasma spray processes also show strong potential to enable the sequential multi-layer depositions of metal-supported fuel cells on porous metallic substrates [19,20].

Plasma spray processing is a well established and proven technology in widespread industrial use for a variety of applications, for instance, the manufactures of coatings to improve wear resistance and mechanical properties [21]. This technology utilizes high temperature plasma flame created by high-voltage electrodes
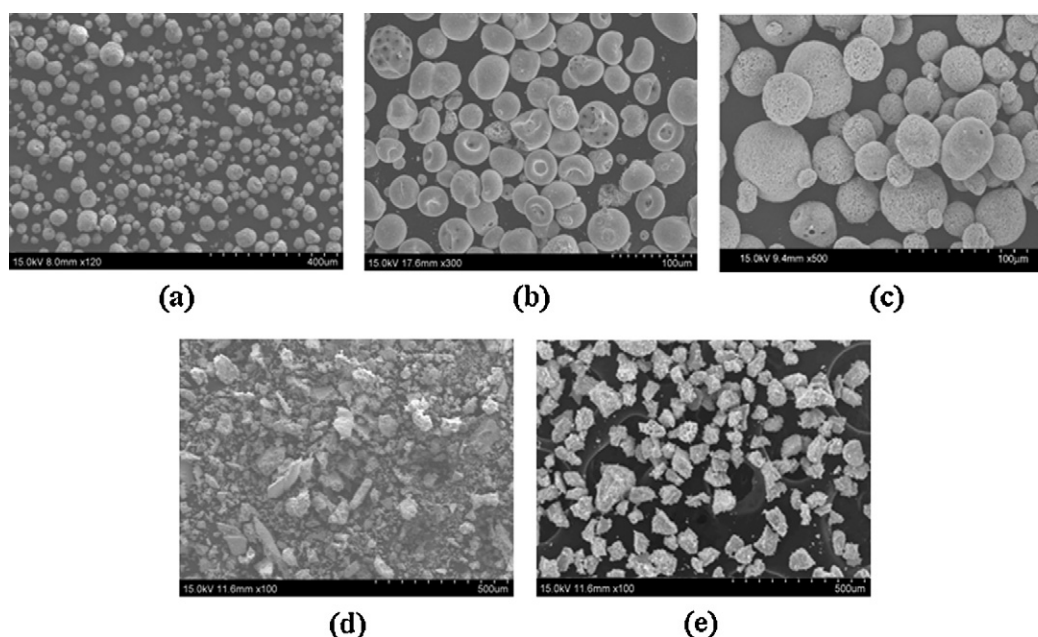
Fig. 1. SEM photos of powders: (a) LDC, (b) LDC/NiO/C, (c) LSCF/C, (d) LSGM and (e) LSCM used to fabricate ITSOFCs.

in the plasma torch to partially or fully melt injected particles that traverse the plasma jet and are deposited on a substrate [22]. Comparing with other existing processes such as chemical vapor deposition, sol–gel method, tape-casting, screen-printing and physical vapor deposition for fabricating SOFC cells [23–31], atmospheric plasma spraying is a fast sintering process, it allows reducing the interaction between layers of SOFC cells that can be induced during conventional high temperature sintering processes, for instance, the interaction between LSGM electrolyte layer and Ni in the anode layer [18,32]. In addition to high material deposition rates, APS processes can easily control the component composition and microstructure through variation of spray parameters, hence, plasma spraying process has thus appeared as a promising candidate for inexpensive and fast cell production, and attracted much attention [18,19,33].

In the development of reduced temperature SOFC technology, reducing electrolyte thickness and developing alternative materials with high ion conductivity at reduced temperatures are two major approaches. The LSGM materials have been reported as a good electrolyte for ITSOFC [34,35]. In our approach, the LSGM($La_{0.8}Sr_{0.2}Ga_{0.8}Mg_{0.2}O_3$) material with high ion conductivity was adopted as an electrolyte in the plasma spray process for obtaining high power density metal-supported ITSOFCs.

2. Experiments

The APS (atmospheric plasma spray) system consists of mainly a modified Praxair SG-100 dc plasma torch with Mach I nozzle that injects a high temperature plasma flame under atmospheric condition, two powder feeder systems for delivering plasma sprayable powders, a cooling system for the torch, a furnace for preheating the substrate, an IR detector for measuring the temperature of the substrate, and a Fanuc Robot ARC Mate 120iB system to scan plasma torch. The modified Praxair SG-100 dc plasma torch with Mach I nozzle is operated at medium currents from 320 to 550 A and at high voltages from 88 to 105 V. The mixed gas from argon, hydrogen and helium is used as plasma forming gas. A specially designed multi-gas mixer is applied to mix these gases uniformly. Other details of experimental apparatus and typical plasma spraying parameters are given in other published papers [36,37].

Commercially available powders of LDC($Ce_{0.55}La_{0.45}O_2$), LDC/NiO/C, LSCF($La_{0.58}Sr_{0.4}Co_{0.2}Fe_{0.8}O_3$)/C, LSGM($La_{0.8}Sr_{0.2}Ga_{0.8}Mg_{0.2}O_3$) and LSCM($La_{0.75}Sr_{0.25}Cr_{0.5}Mn_{0.5}O_3$) as shown in Fig. 1 are applied in this study. LDC, LDC/NiO/C and LSCF/C provided by Inframat Inc., USA are agglomerated powders that have average granule sizes from 20 to 50 μm and can be sprayed directly by APS. Carbon black of 15 wt% is applied as a pore former and it will be burn out during the plasma spray coating. The original particles of LDC and LDC/NiO agglomerated powders are less than 100 nm in size, but the original particles of LSCF agglomerated powders are between 200 nm and 400 nm in size. The Ni content in LDC/NiO/C powders is about 50% in volume after reduction. LSGM and LSCM are sintered and crushed powders, these powders provided by Marion Technologies, France are sieved into a smaller range of powder sizes before plasma spraying. Layers of LSCM, LDC/NiO, LDC, LSGM, LSGM/LSCF and LSCF are sprayed by APS in sequence on a porous nickel substrate with 5 cm in diameter to complete a Ni-LSCM-LDC/NiO-LDC-LSGM–LSGM/LSCF–LSCF cell. The LSGM/LSCF interlayer is formed of LSGM and LSCF with 50%:50% in volume, this layer is applied for matching gradually the thermal expansion coefficients of dense LSGM electrolyte and porous LSCF layer. The porous LSCM layer is applied as an interlayer for minimizing unwanted element diffusion between nickel substrate and nano-structured LDC/NiO anode. The LDC layer is used to inhibit nano nickel particles in the anode to diffuse into LSGM electrolyte and then react with LSGM material. The LSCF layer with 15 cm^2 active area is applied for collecting cell current. To support the whole cells, the nickel substrates with 1.2 mm in thickness are adopted. The NiO can be reduced to Ni by hydrogen gas during the cell test.

The three completed APS cells supported by porous nickel substrates with 3.4, 3.0 and 0.7 Darcy of permeability are prepared for study. They are named as cell A, cell B and cell C. These cells have a nano-structured LDC/Ni anode functional layer, an LDC interlayer, an LSGM electrolyte layer, an LSGM/LSCF cathode interlayer and an LSCF cathode current collector layer. The cell A and cell C have additional LSCM interlayer coated on porous nickel substrates. The cell A is supported by the highest porous nickel substrate with a permeability of 3.4 Darcy, the cell C is supported by the lowest porous nickel substrate with a permeability of 0.7 Darcy, and the
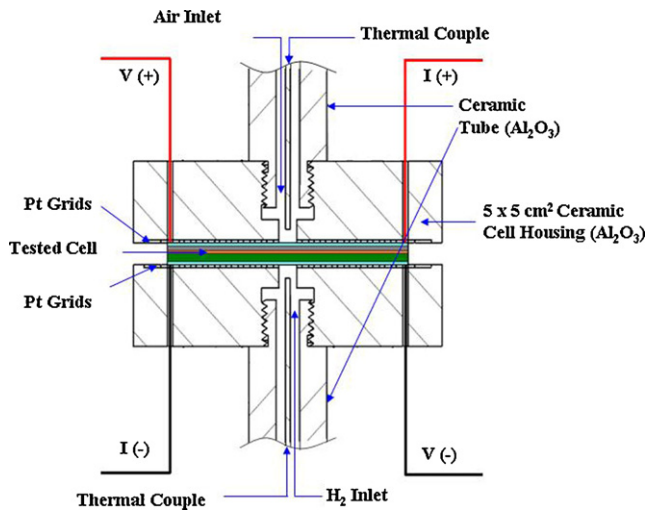
Fig. 2. The scheme of non-sealed cell test housing for measuring cell performance.

cell B having no LSCM interlayer is supported by a porous nickel substrate with a permeability of 3.0 Darcy. The same plasma spray parameters are used to deposit the same physical layers of cell A, cell B and cell C. These cells are measured in a cell performance measurement system with Solartron 1255 and Solartron 1287 for AC impedance measurement and with Prodigit 3311D DC electronic load for power measurement. A non-sealed cell test housing is applied for measuring cell performance. Fig. 2 shows the scheme of non-sealed cell test housing for measuring cell performance. The inert Al_2O_3 ceramic material is used for housing the tested cell. Platinum grids and leads at the anode and cathode side of the cell are used to measure cell current and voltage. Thermocouples close to the anode and cathode of cell are applied to measure temperatures

on both anode and cathode sides. The cell test housing located in an electric furnace is heated up to 800 °C. The inert Al_2O_3 ceramic tubes are used to deliver hydrogen fuel with 335 ml min^{-1} and air oxidizer with 670 ml min^{-1} to the tested cell. The microstructures and EDX analyses of APS cells prepared in this work are observed via SEM (Hitachi S4800) and TEM (FEI Tecnai^{TM} G2 F-20) microscopes.

3. Results and discussion

3.1. Microstructures

Because the same APS spraying parameters are applied for forming cell A, cell B and cell C, the same microstructures of the same layers of these three cells can be assumed and the typical microstructure of cell A are shown here only. Fig. 3a shows the SEM cross sectional micrograph of cell A in a low magnification after hydrogen reduction. The LSGM layer is found to be quite dense with few closed pores and without cracking through. In order to see microstructure details of cell A, the SEM cross sectional micrograph of cell A in a high magnification after hydrogen reduction is given in Fig. 3b. Good interfacial adhesion is found between cell different layers. Fig. 3c gives the EDX line mappings of elements along the selected scan position and direction shown in Fig. 3b, the EDX signals of key elements Co, Fe, Ga, La, Ce, Ni, Mn and Cr versus thickness are given in this figure. The scan direction of line mapping is from cathode to nickel substrate. The thicknesses of different layers shown in Fig. 3b along the selected scan position and direction can be estimated by the EDX signals of these key elements. The EDX signals of Co and Fe elements are used to calculate the total thickness of LSGM/LSCF cathode interlayer plus LSCF current collecting layer, this estimated thickness is around 28 μm. The EDX signals of Ga and Co elements can be used to estimate the LSGM electrolyte thickness which is around 45 μm. The difference between the peak of Ce element EDX signal at about 71 μm and the first peak of Ni
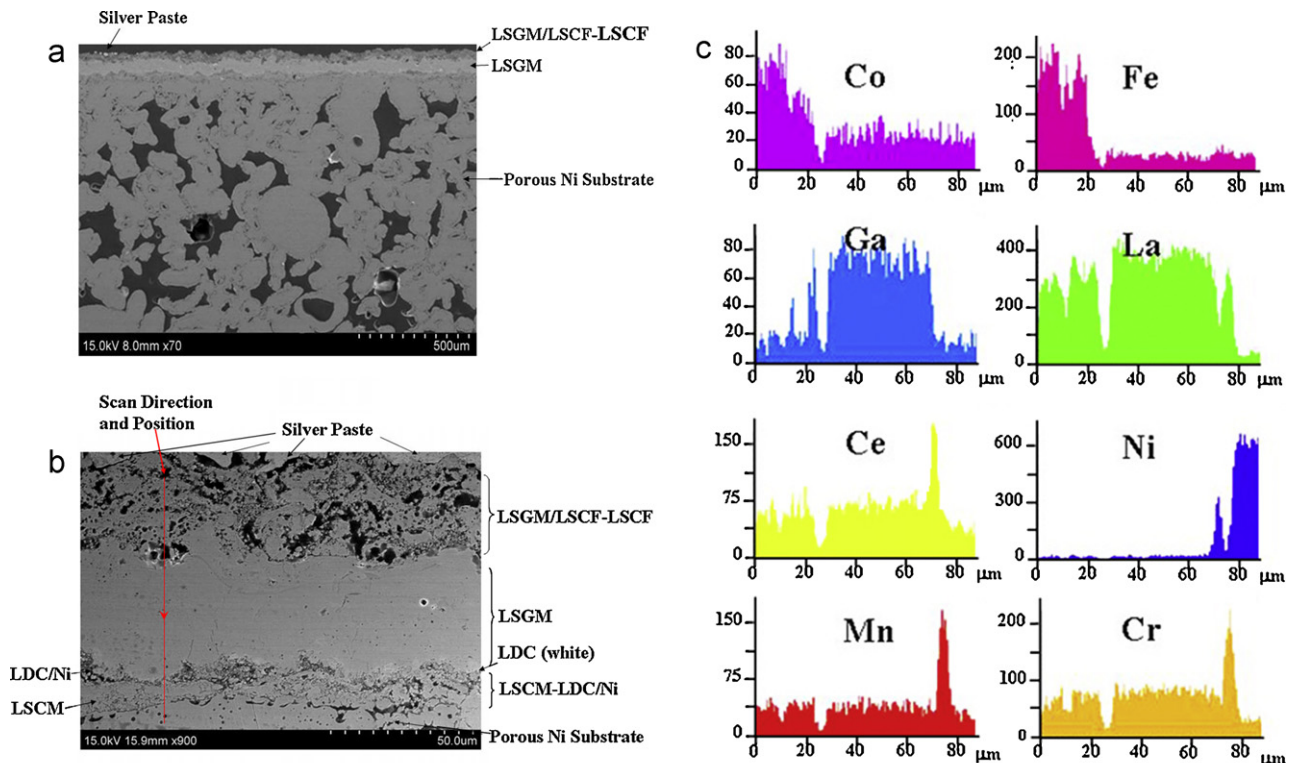

Fig. 3. (a) Cross sectional SEM micrograph of cell A in a low magnification after hydrogen reduction. (b) Cross sectional SEM micrograph of cell A in a high magnification after hydrogen reduction. (c) The EDX line mappings of elements along the selected scan position and direction as shown in (b).
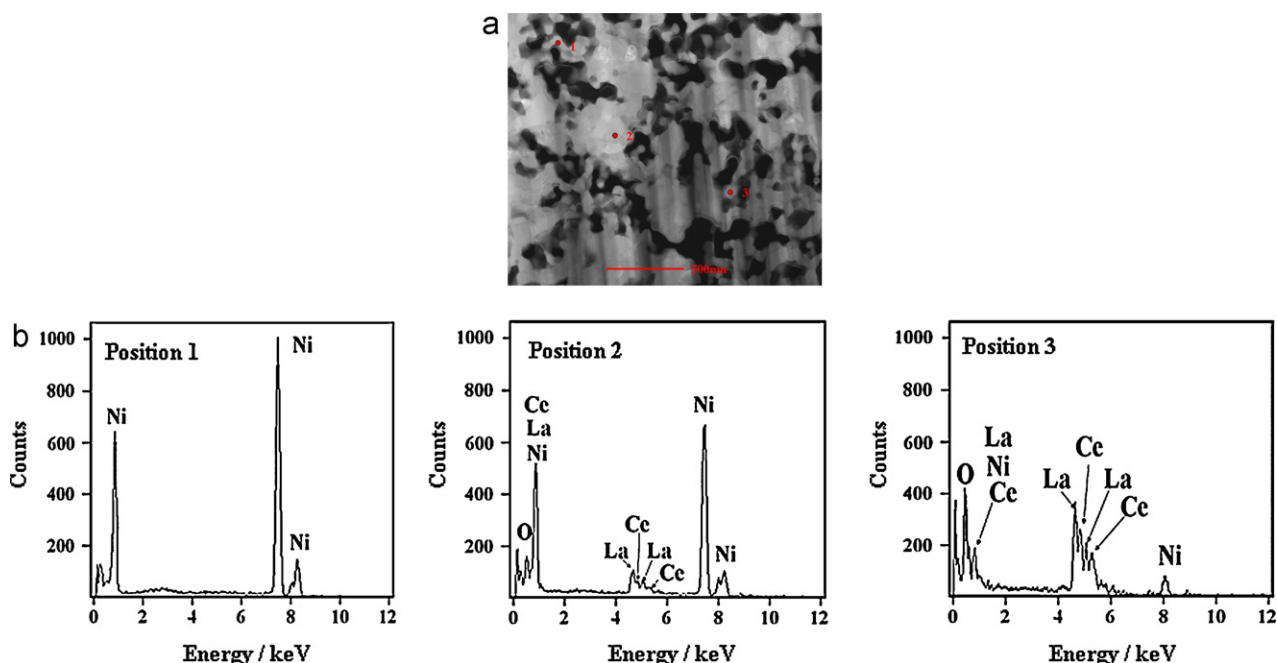
Fig. 4. (a) TEM image of nano-structured LDC/Ni anode in a high magnification. (b) EDX signals at positions of 1, 2 and 3 as shown in (a).

element EDX signal at about 73 μm is used to estimate the LDC interlayer thickness which is around 2 μm. The width measured at the bottom of first peak of Ni element EDX signal is used to estimate the thickness of LDC/Ni anode functional layer. This thickness is about 8 μm. The EDX signal of Mn or Cr is used to estimate the LSCM interlayer thickness which is around 7 μm. Fig. 4a gives the TEM image of nano-structured LDC/Ni anode in a high magnification. The corresponding EDX signals at positions 1, 2 and 3 shown in this figure are given in Fig. 4b. These EDX signals indicate that a nano Ni particle is at the position 1, a cluster of nano Ni particles and nano LDC particles is at the position 2, and a nano LDC particle is preferentially at the position 3. The oxygen EDX signals at positions 2 and 3 are believed to come from LDC particles. This anode contains nano pores, pores larger than 100 nm, nano Ni particles, nano LDC particles and clusters formed by nano Ni particles and nano LDC particles.

3.2. Performances and analyses

Measured I–V–P (Current–Voltage–Power) results of cell A, cell B and cell C at temperatures of 700, 750 and 800 °C are shown in Fig. 5. The hydrogen fuel with 335 ml min^{-1} and the air oxidizer with 670 ml min^{-1} are supplied to the tested cells. All cells have open-circuit voltages (OCVs) which are larger than 1 V so that the LSGM electrolyte prepared by APS process is dense enough and the cell A has the best I–V–P performance. To do further analysis, the cell voltage $V(i)$ can be expressed by [2,8]:

$$V(i) = V_{ocv} - \eta_{ohm} - \eta_{act} - \eta_{con} \tag{1}$$

where V_{ocv} is the open-circuit voltage of cell, $\eta_{ohm} = iR_{ohm}$ is the ohmic overpotential, η_{act} is the activation overpotential and η_{con} is the concentration overpotential. In the I–V–P measurements as shown in Fig. 5, no data below 0.6 V cell voltage are measured and the concentration overpotential η_{con} is usually significant only at low voltages or high current densities so that the measured cell voltages as shown in Fig. 5 can be approximately fitted by:

$$V(i) = V_{ocv} - iR_{ohm} - \eta_{act} \tag{2}$$

When $\eta_{act} \approx a + b\ln(i)$, then Eq. (2) can be rewritten as [2,8]:

$$V(i) = V_{ocv} - iR_{ohm} - (a + b\ln(i)) \tag{3}$$

Table 1
Parameter values in I–V–P analyses for cell A, cell B and cell C at 700, 750 and 800 °C.

Temperature (°C)	V_{ocv} (V)	a	b	R_{ohm} (Ω cm^2)	i_0 (A cm^{-2})	P_{max} (i_{max}) (W cm^{-2})	P_{max} @0.6 V	i_{max} (A cm^{-2})
Cell A								
700	1.08	0.052	0.0153	0.37	0.0334	0.71	0.70	1.383
750	1.066	0.046	0.0146	0.252	0.0425	1.01	0.98	2.004
800	1.049	0.047	0.0152	0.168	0.0454	1.45	1.27	2.934
Cell B								
700	1.052	0.035	0.0096	0.690	0.0270	0.377	0.373	0.7394
750	1.032	0.034	0.0098	0.418	0.0310	0.594	0.575	1.192
800	1.013	0.035	0.011	0.291	0.0434	0.814	0.766	1.673
Cell C								
700	1.052	0.041	0.0084	0.728	0.0077	0.353	0.347	0.6966
750	1.034	0.038	0.0081	0.4725	0.0097	0.525	0.505	1.054
800	1.018	0.041	0.01	0.344	0.0166	0.689	0.634	1.415

a, b and R_{ohm} are fitting values; i_0, $P_{max}(i_{max})$ and i_{max}, are calculated values.
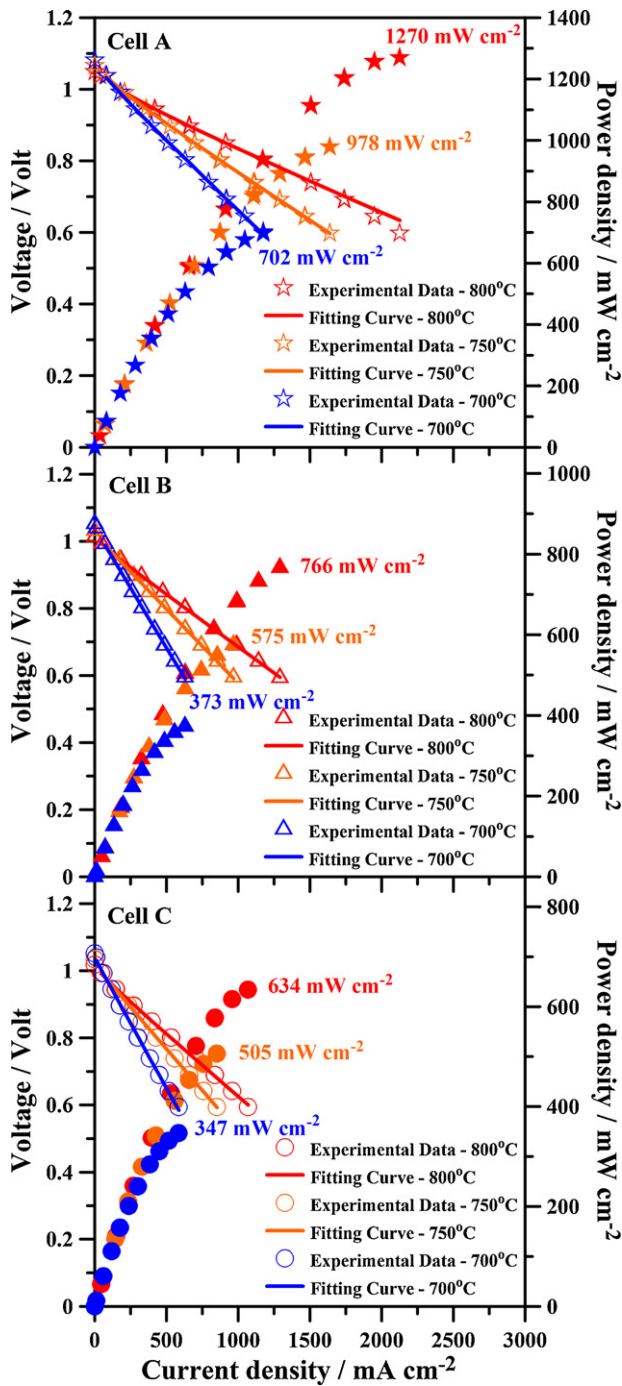P_{max} at 0.6 V and V_{ocv} are experimental values.

Fig. 5. Measured I–V–P results and fitting curves generated by Eq. (3) for cell A, cell B and cell C at temperatures of 700, 750 and 800 °C.

Fig. 5 also gives the fitting curves generated by Eq. (3) for cell A, cell B and cell C at 700, 750 and 800 °C. Eq. (3) cannot be applied for fitting small η_{act} data including OCV (open-circuit voltage) data [8]. For cell B and cell C, all measured I–V data except the data at OCV are fitted very well by Eq. (3). For cell A at 700 and 750 °C, all measured I–V data except the data at OCV are fitted very well by Eq. (3) too, but the measured I–V data at 800 °C are only fitted very well in the current density range from 0.2 A cm^{-2} to 1.5 A cm^{-2}, as the current density becomes larger than 1.5 A cm^{-2}, the deviation between measured I–V data and the fitting curve increases. This deviation can be explained by the increase in the concentration overpotential. The typical value of fitting error χ^2 is less than 10^{-4}.

From the Butler–Volmer equation, the exchange current density i_0 can be expressed by $i_0 \approx \exp(-a/b)$ [2]. The corresponding values of V_{ocv}, R_{ohm}, a, b and i_0 parameters for cell A, cell B and cell C at 700, 750 and 800 °C are given in Table 1. Fig. 6 gives their η_{act} and η_{ohm} curves with respect to current density at these test temperatures. It shows that the ohmic overpotential η_{ohm} is more significant than the activation overpotential η_{act} and $\frac{d\eta_{act}}{di} \approx 0$ at large current densities.

If η_{con} is insignificant, then the power density $P(i)$ can be expressed by the following equation:

$$P(i) = iV(i) \approx iV_{ocv} - i^2 R_{ohm} - i\eta_{act}(i) \tag{4}$$

When $i = i_{max}$, i_{max} is the current density corresponding to the maximum power density $P_{max}(i_{max})$, then:

$$P_{max}(i_{max}) \approx i_{max}(V_{ocv} - \eta_{act}(i_{max})) - i_{max}{}^2 R_{ohm} \tag{5}$$

To find the calculated maximum power densities of cells, $(dP(i)/di)|_{i=i_{max}} = 0$ must hold and, hence:

$$V_{ocv} - 2i_{max}R_{ohm} - \eta_{act}(i_{max}) - i_{max}\frac{d\eta_{act}(i)}{di}\Big|i=i_{max} = 0 \tag{6}$$

Then, $i_{max} = (V_{ocv} - \eta_{act}(i_{max}))/(2R_{ohm} + (d\eta_{act}(i)/di)|_{i=i_{max}})$. This i_{max} can be further simplified to be:

$$i_{max} \approx \frac{(V_{ocv} - \eta_{act}(i_{max}))}{2R_{ohm}} = \frac{(V_{ocv} - a - b\ln(i_{max}))}{2R_{ohm}} \tag{7}$$

where $2R_{ohm} >> d\eta_{act}(i_{max})/di$ or $d\eta_{act}(i_{max})/di \approx 0$ is assumed and it is a good assumption according to Fig. 6. The i_{max} value can be found graphically by intersecting left hand side and right hand side values of Eq. (7). By substituting $i_{max} \approx (V_{ocv} - a - b\ln(i_{max}))/2R_{ohm}$ and $\eta_{act}(i_{max}) \approx a + b\ln(i_{max})$ into Eq. (5), the maximum power density $P_{max}(i_{max})$ can be expressed as:

$$P_{max}(i_{max}) \approx \frac{[V_{ocv} - a - b\ln(i_{max})]^2}{4R_{ohm}} \tag{8}$$

The calculated i_{max} and $P_{max}(i_{max})$ values are also given in Table 1 for comparison. Table 1 shows that for any studied cell the calculated $P_{max}(i_{max})$ values are always larger than the measured P_{max} values at the 0.6 V cell voltage, but as the cell temperature decreases, the R_{ohm} value becomes larger and the difference between calculated $P_{max}(i_{max})$ and measured P_{max} at the 0.6 V cell voltage becomes smaller. Table 1 also shows that the cell A has the smallest R_{ohm} value and can deliver the largest power density for any temperature. Comparing cell A with cell C, Table 1 indicates that the permeability of a substrate for supporting a cell has a significant effect on R_{ohm}, i_0 and then the cell power performance. The cell A with a nickel substrate of 3.4 Darcy permeability has a larger exchange current densities and smaller R_{ohm} values than those of cell C with a nickel substrate of 0.7 Darcy permeability at 700, 750 and 800 °C. The similar phenomenon has been pointed out by A.V. Virkar in the porosity effect of supporting substrate before [2]. Comparing cell A with cell B which is supported by a nickel substrate of 3.0 Darcy permeability, Table 1 indicates that the LSCM layer also has a significant effect on R_{ohm}, i_0 and then the cell power performance. With LSCM layer, the cell R_{ohm} decreases and the exchange current density i_0 increases.

3.3. AC impedances and analyses

Due to the current limit encountered by our AC impedance measurement apparatus, here only the AC impedance data obtained at the OCV condition are analyzed. Other data other than at OCV will be explored in the future. A 10 mV AC signal with a frequency varied from 0.01 Hz to 0.1 MHz is applied in the AC impedance measurements. An AC impedance curve or named as a Nyquist diagram consisting typically of two to three arcs has two intercepts on Z' real
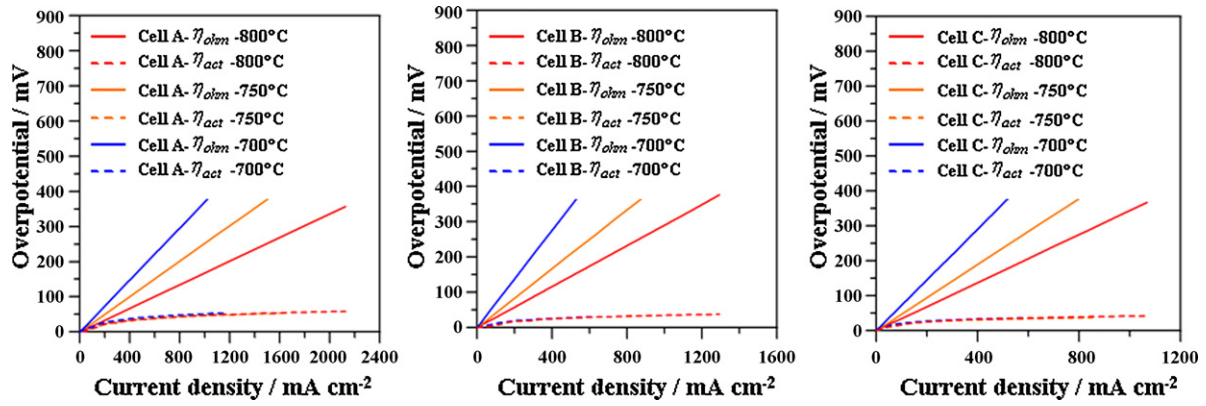
Fig. 6. η_{ohm} and η_{act} for cell A, B and C at 700, 750 and 800 °C.

axis, one is the high frequency intercept R_1, the other is the low frequency intercept R_2 ($\omega \to 0$), the difference between high frequency intercept and low frequency intercept is the total polarization resistance R_p, namely, $R_2 = R_1 + R_p$. R_1 includes the contact resistance, the wire lead resistance and the cell resistance which includes the anode ohmic resistance, the cathode ohmic resistance and the electrolyte ohmic resistance. In this paper, the wire lead resistance is assumed to be negligible and the electrolyte ohmic resistance is dominant in R_1. R_p includes the polarization resistances of the anode and the cathode [8,38,39]. R_1, R_2 and R_p obtained from above Nyquist diagrams are experimentally measured parameters.

Fig. 7 gives the comparisons of AC impedances measured with 335 ml min^{-1} hydrogen fuel and 670 ml min^{-1} air oxidizer at OCV

Fig. 7. The comparisons of AC impedances measured at OCV condition for cell A, cell B and cell C at 700, 750 and 800 °C.

condition for cell A, cell B and cell C. The simplified equivalent circuit of lumped elements L_{lead}, R_e, R_{ap}, R_{cp}, C_a, C_c, W_s as shown in Fig. 7 is applied to analyze the AC impedance curves consisting of two arcs [36,40]. The fitting curves generated by this simplified equivalent circuit are also given in this figure. The fitting curves match the experimental data very well with a fitting χ^2 error about 10^{-4}. In this simplified equivalent circuit, L_{lead} is the lead inductance, R_e is the electrolyte ohmic resistance, R_{ap} is the polarization resistance of the anode, R_{cp} is the polarization resistance of cathode, C_a represents the polarization capacitance of anode, C_c represents the polarization capacitance of cathode and W_s is the finite length Warburg short circuit terminus that simulates oxygen oxidant mass transport and diffusion process in the cathode [41–43]. L_{lead}, R_e, R_{ap}, R_{cp}, C_a, C_c, and W_s are fitting parameters, their values are obtained from above curve fittings. The impedance $Z_{ws}(\omega)$ of finite length Warburg short circuit terminus W_s can be expressed by the following equation:

$$Z_{ws}(\omega) = \frac{W_{s-r} \times \tanh([i \times W_{s-t} \times \omega]^{W_{s-p}})}{(i \times W_{s-t} \times \omega)^{W_{s-p}}} \tag{9}$$

where ω is the frequency, $i = \sqrt{-1}$, W_{s-t} and W_{s-p} are dimensionless fitting parameters, and W_{s-r} is the fitting parameter in $\Omega\,cm^2$ unit [36,43]. As ω approaches to zero, $Z_{ws}(\omega)$ approaches to W_{s-r}. In this simplified equivalent circuit model, the layers of LSGM/LSCF and LSCF are combined together and assumed to act as a cathode, the AC impedance behavior of this cathode is simulated by R_{cp}, C_c and W_s lumped elements. The layers of LSGM and LDC are combined together and assumed to act as an electrolyte, the AC impedance behavior of this electrolyte is simulated by R_e lumped element. For cell A and cell C, the layers of LSCM and LDC/Ni are combined together and assumed to act as an anode, the AC impedance behavior of this anode is simulated by R_{ap} and C_a lumped elements. For cell B, the anode contains only LDC/Ni layer, the AC impedance behavior of this anode is simulated by R_{ap} and C_a lumped elements. The resistance of nickel substrate is neglected in this model. The nickel substrate just plays the roles of cell support and gas distributor. The nickel substrate with a high permeability supplies more gases to the anode than the nickel substrate with a low permeability. The mass transport and diffusion of hydrogen in the nickel substrate and anode are not simulated in this simplified equivalent circuit model. In other words, it is assumed that the anode reaction kinetics is fast compared to the cathode reaction kinetics.

As the temperature of the cell increases, the AC impedances for all tested cells move towards lower values on the real $Z'(\Omega\,cm^2)$ axis. The cell A has the smallest values of high frequency and low frequency intercepts among the tested cells at temperatures of 700, 750 and 800 °C, respectively. Because only resistances of a cell can consume energy and affect the cell power performance, the values
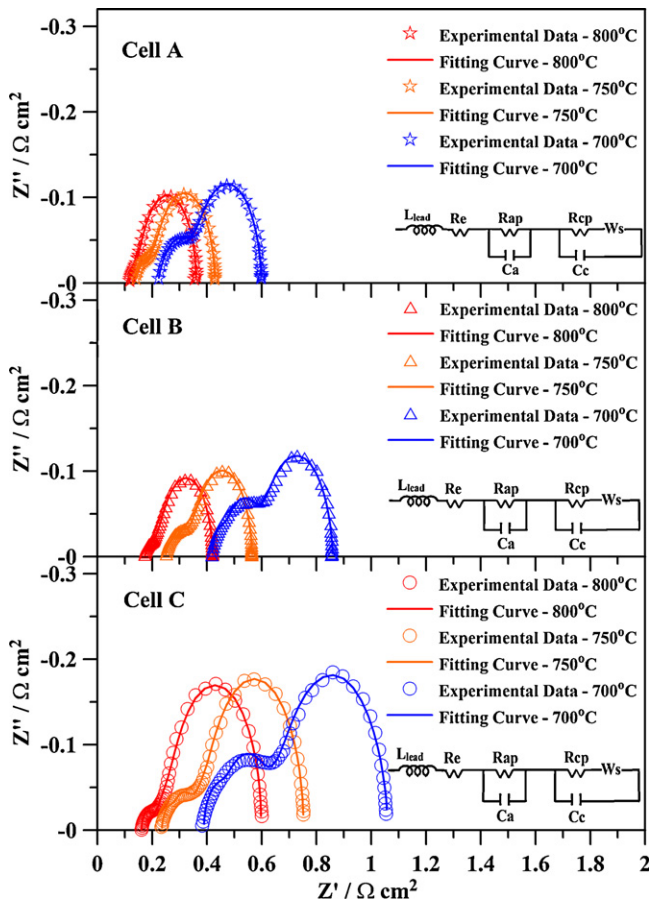
Table 2
The values of R_1, R_2, R_p, R_e, R_{ap}, R_{cp} and W_{s-r} parameters at test temperatures of 700, 750 and 800 °C.

Temperature (°C)	R_1 ($\Omega\,cm^2$)	R_2 ($\Omega\,cm^2$)	R_p ($\Omega\,cm^2$)	R_e ($\Omega\,cm^2$)	R_{ap} ($\Omega\,cm^2$)	R_{cp} ($\Omega\,cm^2$)	W_{s-r} ($\Omega\,cm^2$)	$R_e + W_{s-r}$
Cell A								
700	0.21	0.602	0.392	0.205	0.037	0.077	0.28	0.485
750	0.137	0.432	0.295	0.122	0.015	0.038	0.252	0.374
800	0.115	0.37	0.255	0.103	0.010	0.005	0.242	0.345
Cell B								
700	0.418	0.855	0.437	0.415	0.084	0.053	0.306	0.721
750	0.25	0.563	0.313	0.245	0.034	0.027	0.259	0.504
800	0.172	0.42	0.248	0.162	0.015	0.013	0.231	0.393
Cell C								
700	0.38	1.054	0.674	0.386	0.114	0.077	0.484	0.87
750	0.233	0.752	0.519	0.236	0.049	0.041	0.428	0.664
800	0.161	0.6	0.439	0.163	0.017	0.025	0.390	0.553

R_1, R_2 and R_p are experimentally measured parameters at OCV condition.
R_e, R_{ap}, R_{cp}, and W_{s-r} are fitting parameters.

of R_1, R_2, R_p, R_e, R_{ap}, R_{cp}, W_{s-r} at test temperatures of 700, 750 and 800 °C are given in Table 2 for comparison. From the values shown in Table 2, $R_1 \approx R_e$, $R_p \approx R_{ap} + R_{cp} + W_{s-r}$ and $R_2 \approx R_e + R_{ap} + R_{cp} + W_{s-r}$ are found, and R_{ap} and R_{cp} polarization resistances are smaller than W_{s-r} for all tested cells. This table also shows that W_{s-r} and R_e are two major internal resistances of cells for energy losses. The sum of R_e and W_{s-r} obtained at OCV condition is also shown in Table 2. The plots of $R_e + W_{s-r}$ and P_{max} at the 0.6 V versus temperature are given in Fig. 8. This figure shows that $R_e + W_{s-r}$ decrease as the cell's temperature increases. The variation trend of $R_e + W_{s-r}$ can be explained by the increases in the electrolyte conductivity and by the increases in the oxygen oxidant transport-diffusion rate in the cathode with respect to the increase of temperature [1,38,44]. This figure also shows that the maximum power density P_{max} at the 0.6 V increases as $R_e + W_{s-r}$ decreases. Among cells tested at 700, 750 and 800 °C, at any test temperature the cell A having the smallest value of $R_e + W_{s-r}$ has the highest power output and the cell C having the largest value of $R_e + W_{s-r}$ has the lowest power output.

3.4. Durability test

Here, only the cell A which has the best power performance was tested during 1000 h. The results of this durability test are given in Fig. 9. This cell was tested at 700 °C under 400 mA cm^{-2} constant current density, 335 ml min^{-1} hydrogen fuel and 670 ml min^{-1} air oxidizer flow rates. From the observed variations of voltage and power shown in Fig. 9, the estimated degradation rate is about 3% kh^{-1}. As shown in Fig. 2, the cell test apparatus contains Pt grids
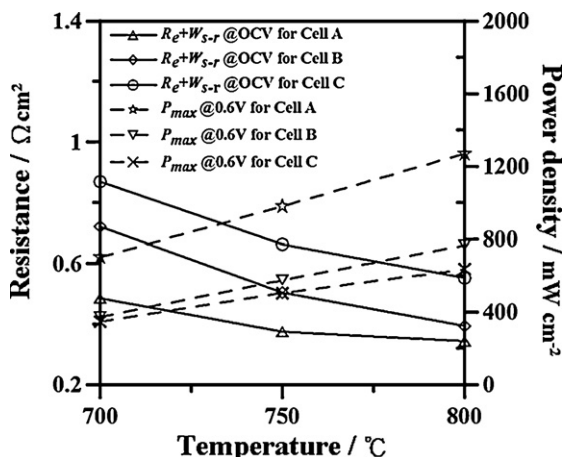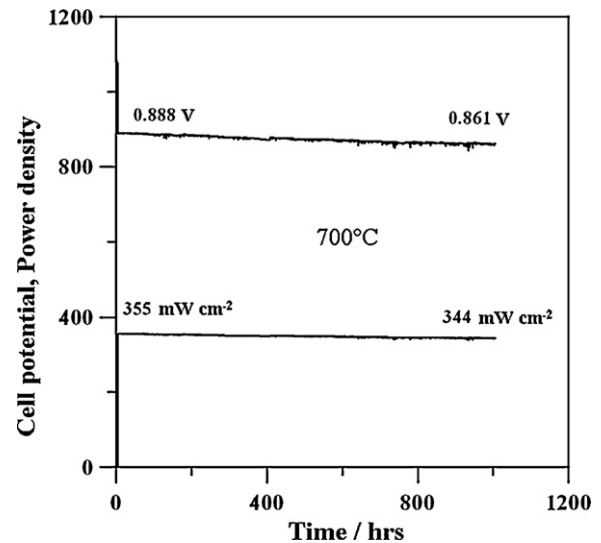
Fig. 9. Variations of voltage and power of cell A for the time period of 1000 h.

and ceramic cell housings that are close to tested cells and are believed to be stable; therefore, the degradation contributed by the test apparatus should be negligible. During this long durability test, no nitrogen gas is applied at the anode side of cell to blow off the water vapor which can be accumulated in the anode and may affect the voltage and power performances of cell A. This effect is included in this estimated degradation rate. The actual degradation rate due to cell's material and structure changes should be less than 3% kh^{-1}. The power and degradation performances of cell A indicate that the performance of plasma sprayed metal-supported cell Ni-LSCM-LDC/Ni-LDC-LSGM-LSGM/LSCF-LSCF type is comparable with other metal-supported cells published in the literature [16,17,35,45].

4. Conclusions

Three different metal-supported intermediate temperature solid oxide fuel cells (ITSOFCs) were prepared by APS technology and tested to obtain their I–V–P data and AC impedances at OCV condition. These cells with 5 cm in diameter have a nano-structured LDC/Ni anode functional layer, an LDC interlayer, an LSGM electrolyte layer, an LSGM/LSCF cathode interlayer and an LSCF cathode current collector layer with 15 cm^2 active area. Two of these cells have additional LSCM interlayer coated on porous nickel substrates. From I–V–P data and related analyses, it is found that the cell supported by a highly porous nickel substrate with

Fig. 8. The plots of $R_e + W_{s-r}$ and P_{max} at the 0.6 V versus temperature.

a permeability of 3.4 Darcy and having LSCM interlayer on this nickel substrate has the best power performance, the smallest R_{ohm} and the largest exchange current density i_0. At 700, 750 and 800 °C test temperatures, this cell can deliver 702, 978 and 1270 mW cm^{-2} maximum power densities at the 0.6 V cell voltage respectively under 335 ml min^{-1} H$_2$ and 670 ml min^{-1} air flow rates. The analytic formula for calculating $P_{\max}(i_{\max})$ is derived here. The difference between calculated $P_{\max}(i_{\max})$ and measured $P_{\max}$ at the 0.6 V cell voltage is small at low test temperatures, such as 700 and 750 °C, but it becomes larger at 800 °C. For these cells prepared by APS process, the energy loss through R_{ohm} resistance is more significant than the activation losses of electrodes. From AC impedance data obtained at OCV condition and related analyses of simplified equivalent circuit model, the electrolyte resistance R_e and the cathode oxygen oxidant mass transport and diffusion resistance W_{s-r} are two major internal resistances of cells that consume energy. The cell that has the smallest value of $R_e + W_{s-r}$ has the highest power output, the cell that has the largest value of $R_e + W_{s-r}$ has the lowest power output. Therefore, in the future work, reducing the thickness of LSGM electrolyte and improving the microstructures of LSGM/LSCF cathode interlayer and LSCF cathode current collector layer are the main keys to optimize the power performance of APS prepared cells.

Finally, under 400 mA cm^{-2} constant current density condition, the cell with the best power performance exhibits about 3% kh^{-1} degradation rate of measured voltage or power at 700 °C for the time period of 1000 h. The further study on the degradation mechanism is needed for reducing this degradation rate. But, the results presented in this paper show that the APS technology applied for fabricating all layers of metal-supported and LSGM based ITSOFCs is promising.

Acknowledgements

References

[1] S.C. Singhal, K. Kendall, High Temperature Solid Oxide Fuel Cell, Elsevier, 2004.
[2] F. Zhao, A.V. Virkar, J. Power Sources 141 (2005) 79–95.
[3] M.C. Williams, J. Strakey, W. Surdoval, J. Power Sources 159 (2006) 1241–1247.
[4] J.P.P. Huijsmans, Curr. Opin. Solid State Mater. Sci. 5 (2001) 317–323.
[5] S.M. Haile, Acta Mater. 51 (2003) 5981–6000.
[6] N.Q. Minh, Solid State Ionics 174 (2004) 271–277.
[7] L. Blum, W.A. Meulenberg, H. Nabielek, R. Steinberger-Wilckens, Int. J. Appl. Ceram. Technol. 2 (6) (2005) 482–492.
[8] W. Gong, S. Gopalan, U.B. Pal, J. Power Sources 160 (2006) 305–315.
[9] K. Föger, J.G. Love, Solid State Ionics 174 (2004) 119–126.
[10] D.J.L. Brett, P. Aguiar, N.P. Brandon, R.N. Bull, R.C. Galloway, G.W. Hayes, K. Lillie, C. Mellors, C. Smith, A.R. Tilley, J. Power Sources 157 (2006) 782–798.
[11] S. Kakaç, A. Pramuanjaroenkij, X.Y. Zhou, Int. J. Hydrogen Energy 32 (2007) 761–786.
[12] Z. Wang, J.O. Berghaus, S. Yick, C. Decès-Petit, W. Qu, R. Hui, R. Maric, D. Ghosh, J. Power Sources 176 (2008) 90–95.
[13] M.C. Tucker, G.Y. Lau, C.P. Jacobson, L.C. DeJonghe, S.J. Visco, J. Power Sources 175 (2008) 447–451.
[14] M.C. Tucker, J. Power Sources 195 (2010) 4570–4582.
[15] C. Lee, J. Bae, J. Power Sources 176 (2008) 62–69.
[16] T. Ishihara, J. Yan, M. Enoki, S. Okada, H. Matsumoto, J. Fuel Cell Sci. Technol. 5 (2008) 031205-1–131205-3.
[17] R. Hui, J.O. Berghaus, C. Decès-Petit, W. Qu, S. Yick, Jean-Gabriel Legoux, C. Moreau, J. Power Sources 191 (2009) 371–376.
[18] R. Hui, Z. Wang, O. Kesler, L. Rose, J. Jankovic, S. Yick, R. Maric, D. Ghosh, J. Power Sources 170 (2007) 308–323.
[19] R. Henne, J. Therm. Spray Technol. Vol.16 (3) (2007) 381–403.
[20] X.C. Lu, J.H. Zhu, J. Power Sources 165 (2007) 678–684.
[21] O. Kesler, J. Matejicek, S. Sampath, S. Suresh, T. Gnaeupel-Herold, P.C. Brand, H.J. Prask, Mater. Sci. Eng. A257 (1998) 215–224.
[22] P. Fauchais, J. Phys. D: Appl. Phys. 37 (2004) R86–R108.
[23] G. Meng, H. Song, Q. Dong, D. Peng, Soild State Ionics 175 (2004) 29–34.
[24] Y. Liu, M. Liu, J. Am. Ceram. Soc. 87 (2004) 2139–2142.
[25] J. Will, A. Mitterdorfer, C. Kleinlogel, D. Perednis, L.J. Gauckler, Solid State Ionics 131 (2000) 79–96.
[26] L.R. Pederson, P. Singh, X.D. Zhou, Vacuum 80 (2006) 1066–1083.
[27] J.L. Young, T.H. Etsell, Solid State Ionics 135 (2000) 457–462.
[28] S. Zha, Y. Zhang, M. Liu, Solid State Ionics 176 (2005) 25–31.
[29] D. Simwonis, H. Thulen, F.J. Dias, A. Naoumidis, D. Stover, J. Mater. Process. Technol. 92–93 (1999) 107–115.
[30] J. Van herle, R. Ihringer, R. Vasquez Cavieres, L. Constantin, O. Bucheli, J. Eur. Ceram. Soc. 21 (2001) 1855–1859.
[31] N. Jordan, W. Assenmacher, S. Uhlenbruck, V.A.C. Haanappel, H.P. Buchkremer, D. Stöver, W. Mader, Solid State Ionics 179 (2008) 919–923.
[32] X. Zhang, S. Ohara, H. Okawa, R. Maric, T. Fukui, Solid State Ionics 139 (2001) 145–152.
[33] O. Kesler, Mater. Sci. Forum. 539–543 (2007) 1385–1390.
[34] F. Bozza, R. Polini, E. Traversa, Electrochem. Commun. 11 (2009) 1680–1683.
[35] R. Vaßen, D. Hathiramani, J. Mertens, V.A.C. Haanappel, I.C. Vinke, Surf. Coat. Technol. 202 (2007) 499–508.
[36] C.S. Hwang, C.H. Tsai, C.H. Lo, C.H. Sun, J. Power Sources 180 (2008) 132–142.
[37] C.H. Lo, C.H. Tsai, C.S. Hwang, Int. J. Appl. Ceram. Technol. 6 (4) (2009) 513–524.
[38] W. Gong, S. Gopalan, U.B. Pal, J. Mater. Eng. Perform. 13 (2004) 274–281.
[39] K.J. Yoon, P. Zink, S. Gopalan, U.B. Pal, J. Power Sources 172 (2007) 39–49.
[40] R.P. O'hayre, S.W. Cha, W. Colella, F.B. Prinz, Fuel Cell Fundamentals, John Wiley & Sons Inc., New York, USA, 2006.
[41] E. Lust, P. Möller, I. Kivi, G. Nurk, S. Kallip, P. Nigu, K. Lust, J. Electrochem. Soc. 152 (2005) A2306–A2308.
[42] M.A. Rolando, Roque-Malherbe, The Physical Chemistry of Materials: Energy and Environmental Applications, CRC Press, Boca Raton, FL, USA, 2009.
[43] ZPlot for Windows-Electrochemical Impedance Software Operating Manual, Chapter 8, Scribner Associates, Inc., NC, USA, 2000.
[44] J.W. Fergus, R. Hui, X. Li, D.P. Wilkinson, J. Zhang, Solid Oxide Fuel Cells: Materials Properties and Performance, CRC Press, Boca Raton, FL, USA, 2009.
[45] Z. Bi, B. Yi, Z. Wang, Y. Dong, H. Wu, Y. She, M. Cheng, Electrochem. Solid. State Lett. 7 (5) (2004) A105–A107.